# Supplementary Information: Interplay of filling fraction and coherence in symmetry broken graphene p-n junction

Arup Kumar Paul[1], Manas Ranjan Sahu[1], Chandan Kumar[1], Kenji Watanabe[2], Takashi Taniguchi[2] and

Anindya Das[1]

[1]*Department of Physics, Indian Institute of Science, Bangalore, 560012, India.*
[2]*National Institute for Materials Science, Namiki 1-1, Ibaraki 305-0044, Japan.*

Supplementary Note 1 : Device fabrication and device structure
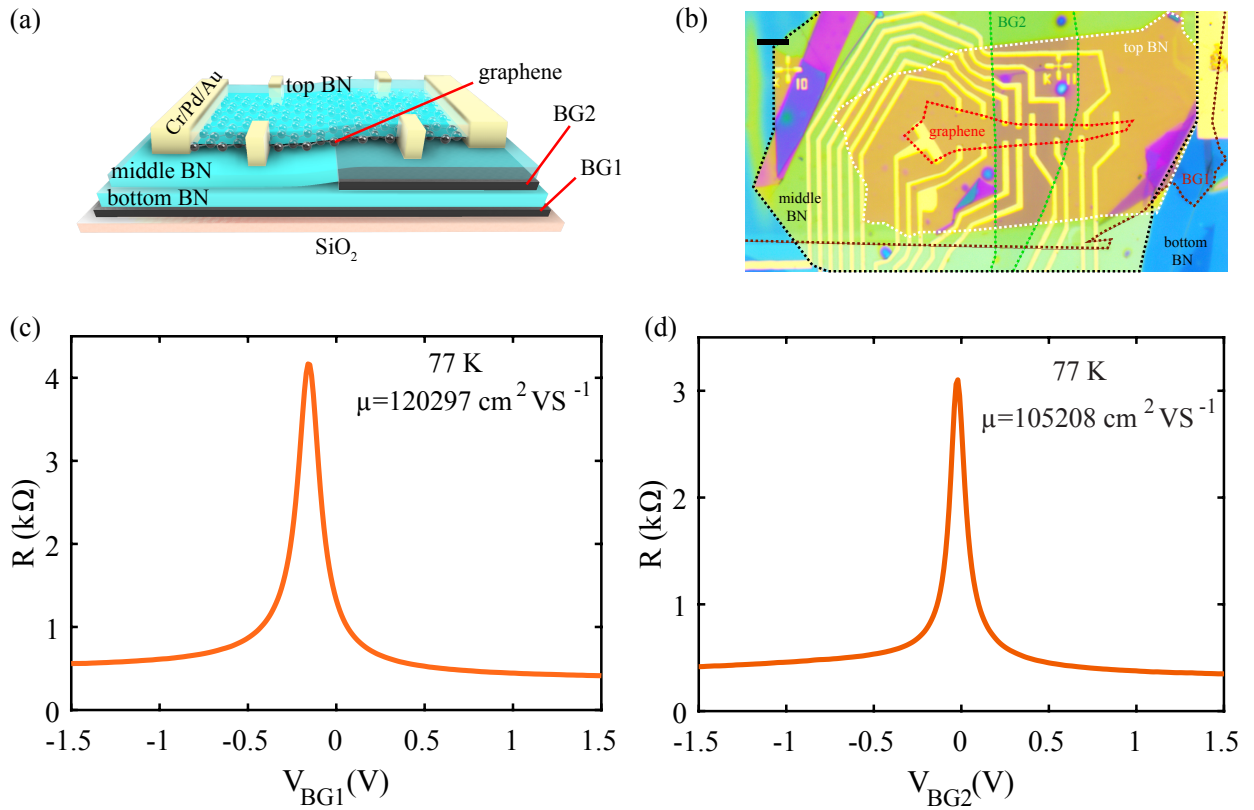
Supplementary Figure 1 Schematics and zero magnetic field response. (a) The schematics of the device and (b) optical image of the measured device. In the optical image, the graphene flake, the graphite gates BG2 and BG1 are shown respectively by the areas enclosed by red, green and brown lines. The top and middle BN is shown by the white and black dashed line enclosed areas. The bottom BN covers the entire picture. The scale bar is $10\mu m$. (c) and (d) shows the zero magnetic field gate response of the $BG1$ and $BG2$ side, respectively, at 77 K. Mobility for both side is found to be of the oreder of $10^5 cm^2 V s^{-1}$.

The device structure is shown in Supplementary Figure 1(a) and the optical image of the measured device is shown in Supplementary Figure 1(b). The device consists of three hexagonal boron nitride (BN) flakes. The top ($\sim 15nm$) and the middle ($\sim 21nm$) BN encapsulate the graphene flake, while the bottom BN ($\sim 30nm$) isolates the two bottom graphite gates BG1 and BG2. The gate $BG2$ covers half of the graphene flake, thus it can only control the density of the region above it. Similarly the gate $BG1$ controls the density of the other half and can not effect the region above $BG2$ due to screening. The entire stack of encapsulated graphene and bottom graphite gates were assembled using the well known hot pick-up and transfer technique[1, 2, 3]. The edge contacts on the graphene flake were first defined by e-beam lithography and then realized by reactive ion etching (RIE) and subsequent deposition of $Cr(2nm)$, $Pd(10nm)$ and $Au(70nm)$ by thermal evaporation.

**Supplementary Note 2 : Conductance and shot noise measurement setup**
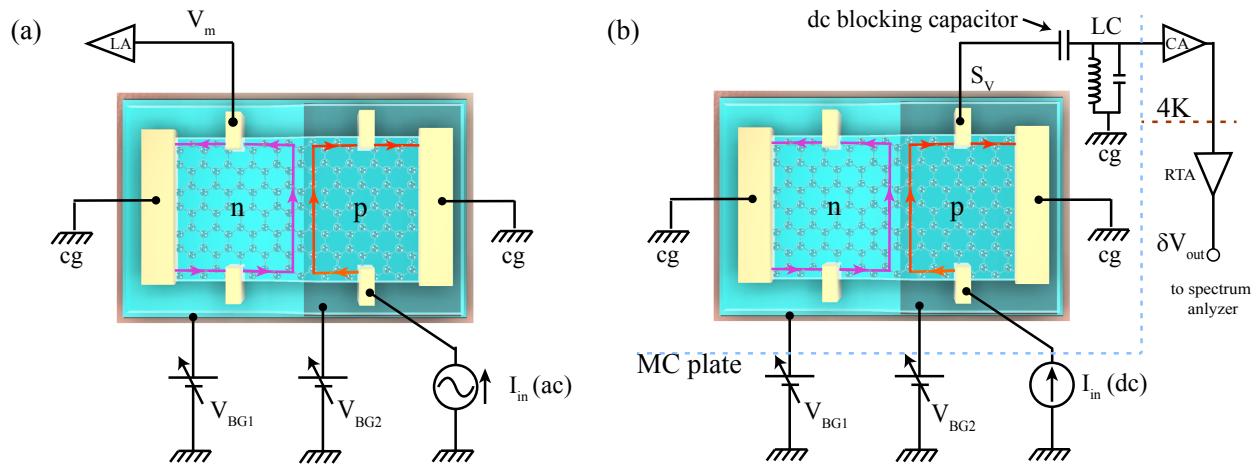
Supplementary Figure 2   Measurement setup. (a) Low frequency conductance measurement setup. Low frequency AC current is injected at p side and the transmitted current I_t at n side is determined by measuring the voltage V_m. (b) Shot noise measurement setup. For this measurement I_{in} is a DC current and the noise is measured at the reflection side (p-side). The segment of the measurement setup sitting in the dilution mixing chamber plate (MC plate) is shown by the blue dashed line. The HEMT cryo-amplifier is at the dilution 4K plate as shown by the brown dashed line. All the gate voltage, current injection and voltage measurement lines (line for measuring V_m in Supplementary Figure 2(a)), which directly goes form room temperature to the MC pate, passes through a RC low pass filter followed by silver powder filter.

The measurement setup consists of a low-frequency conductance and a shot noise measurement parts, which are shown separately in Supplementary Figure 2(a) and 2(b), respectively. For both the measurements, in the bipolar regime the current I_{in} is injected at p side. At the junction I_{in} is partitioned among the co-propagating edge states. For junction transmittance measurement, low frequency Lock-in technique is used. In this case I_{in} is low frequency ac excitation (13 Hz). To find transmittance (t) , the voltage drop V_m created due to the transmitted current I_t going to the left cold ground, is measured by a lock-In amplifier. Hence t is determined from V_m as $V_m = I_t/|\nu_n|\frac{e^2}{h}$, where ν_n is the filling factor of n side.

The partitioning of I_{in} along the pn junction generates shot noise, which is carried by outgoing edge states on both n (transmitted) and p (reflected) side. We have measured the noise at the p-side as shown in Supplementary Figure 2(b). The setup utilizes a well known resonant circuit based noise measurement scheme [4], which consists of a LC resonant circuit, followed by a high electron mobility transistor (HEMT) based cryo-amplifier (CA) sitting at the $4K$ plate of the dilution, and then a room temperature amplifier (RTA) and spectrum analyzer. The L of the resonant circuit is an inductor coil of superconducting wire and the parallel capacitor C is the total capacitance of the co-axial cable connecting from the sample to the CA. The noise is always measured at the LC resonance frequency (~ 765 kHz), which is verified by thermal noise measurement as described later. The measured voltage noise $S_V(f) = <\delta V_{out}(f)>^2/(BW * A^2)$, where δV_{out} is the rms value of the output of the CA-RTA amplifier chain, BW is the measurement bandwidth (for our case $\sim 30kHz$) and A is the total gain of the amplifier chain. S_V is then converted to current noise $S_I = S_V/R^2$, where R is the quantum resistance of the p as given by $R = |\nu_p|\frac{e^2}{h}$, where ν_p is the filling factor of the p side.

**Supplementary Note 3 : Quantum Hall response of p and n side**
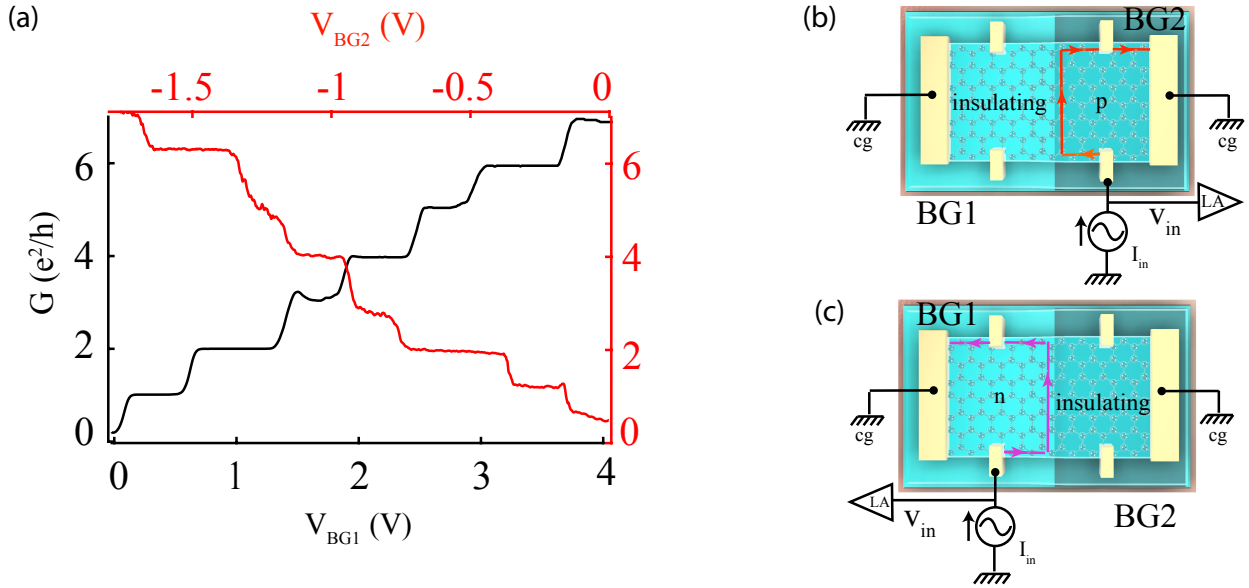
Supplementary Figure 3   Quantum Hall response. (a)The conductance versus gate voltage (V_{BG1} and V_{BG2}) responses, of the p and n side showing quantized conductance plateaus, at magnetic field $8T$ are shown by the red and black lines, respectively. (b) and (c) are experimental setup to measure the quantum Hall (QH) responses of p and n side, respectively. In both the cases the voltage drop (V_{in}) at the injection lead is used for measuring the QH responses. For a fixed I_{in} ($\sim 5nA$), $V_{in} = I_{in}R_{p,n}$, where $R_p(R_n)$ is the quantum resistance seen at injection lead at p (n) side. R_p and R_n depends on the gate voltages V_{BG2} and V_{BG1}, respectively.

The individual QH responses of p and n side at magnetic field $8T$ are shown in Supplementary Figure 3(a). As can be seen, all the symmetry broken QH plateaus corresponding to conductance $G_{p,n} = |\nu_{p,n}|\frac{e^2}{h}$, are clearly distinguishable. Here $\nu_{p,n}$ corresponds symmetry broken filling factor $\pm 1, \pm 2, \pm 3, \pm 4...$ etc. Supplementary Figure 3(a) and 3(b) show the configurations used to measure the individual responses of p

3

and n side, respectively, while the other side of the pn junction was kept at insulating sate. In both the cases the voltage drops (V_{in}) were measured at the injection probe as shown in the figures. The response of the bipolar regime of the pn junction is shown in the manuscript (Fig. 1b).

Supplementary Note 4 : Junction transmittance for different spin models
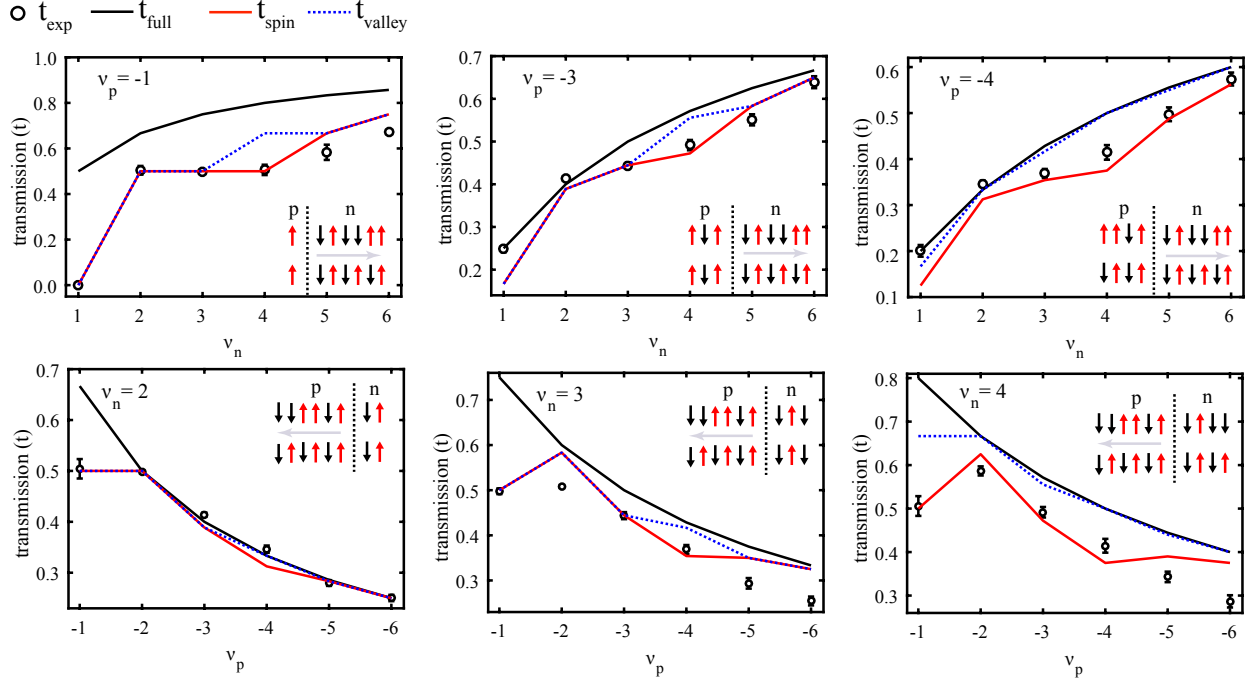
Supplementary Figure 4   transmittance versus filling factor. Comparison of experimentally measured junction transmittance t (open circles with errorbars) as function of p and n side filling factors ν_p and ν_n, with theoretically calculated values for full equilibration (black) and spin selective equilibration with spin configurations of spin-polarized (red solid line) and valley-polarized (blue dashed line) ground states. The errorbars represents the standard deviation of the transmittance from the average values. In the insets, the spin structure of the co-propagating edge states has been shown for spin-polarized (top) and valley-polarized (bottom) ground states.

In Supplementary Figure 4 we have plotted the experimentally determined junction transmittance (t) (open circles with errorbars) as function of filling factor ν_n (top panel) and ν_p (bottom panel). To understand the filling factor dependence of t we compare the experimental values with corresponding theoretically calculated value considering full and spin selective equilbration of the edge states at the pn junction. In our measurement configuration (Supplementary Figure 2(a)) a part of current injected I_{in} at the p side transmits to the n side. In case of full equilbration I_{in} is equally distributed among the co-propagating edge states coming from both side. Hence after equilbration the current carried by each of the edge states is $I_{in}/(|\nu_p| + |\nu_n|)$. As n side has $|\nu_n|$ number of out going edge channels, the net transmitted current I_t, for full equilibration is $I_t = I_{in}(|\nu_n|/(|\nu_p| + |\nu_n|))$. Hence transmittance $t = |\nu_n|/(|\nu_p| + |\nu_n|)$. The calculated values for full equilibration is plotted as solid black lines in Supplementary Figure 4. In case of spin selective equilibration, first the injected current is divided between the up and down spin channels. If $|\nu_{p\uparrow}|$ and $|\nu_{p\downarrow}|$

are the number of up and down spin edge states at the p side then the current carried by the up and down spin channels at the p-side is $I_{in\uparrow} = (|\nu_{p\uparrow}|/|\nu_p|)I_{in}$ and $I_{in\downarrow} = (|\nu_{p\downarrow}|/|\nu_p|)I_{in}$, respectively. At the pn junction considering the equilibration between the same type of spin, the transmitted current for up and down spin channel is $I_{t\uparrow} = (|\nu_{n\uparrow}|/(|\nu_{n\uparrow}| + |\nu_{p\uparrow}|))I_{in\uparrow}$ and $I_{t\downarrow} = (|\nu_{n\downarrow}|/(|\nu_{n\downarrow}| + |\nu_{p\downarrow}|))I_{in\downarrow}$, where $|\nu_{n\uparrow}|(|\nu_{n\downarrow}|)$ are the number of up (down) spin edge states at the n side. Hence the net transmitted current $I_t = I_{t\uparrow} + I_{t\downarrow}$ can be written as $I_t = (|\nu_{n\uparrow}|/(|\nu_{n\uparrow}| + |\nu_{p\uparrow}|))I_{in\uparrow} + (|\nu_{n\downarrow}|/(|\nu_{n\downarrow}| + |\nu_{p\downarrow}|))I_{in\downarrow}$. Therefore, after using the expression for $I_{in\uparrow}$ and $I_{in\downarrow}$, the junction transmittance is given by $t = (1/|\nu_p|)[(|\nu_{p\uparrow}\nu_{n\uparrow}|)/(|\nu_{p\uparrow}| + |\nu_{n\uparrow}|) + (|\nu_{p\downarrow}\nu_{n\downarrow}|)/(|\nu_{p\downarrow}| + |\nu_{n\downarrow}|)]$. The calculated values using this expression for two different spin structure are shown by red solid lines (spin-polarized) and blue dashed line (valley-polarized) in Supplementary Figure 4. As can be seen from the comparison, the filling factor dependence of t, can be well understood by the spin selective equilibration model, more specifically for the spin-polarized ground state structure. In the insets of Supplementary Figure 4 we have shown the spin structure of the co-propagating edge states at the junction for spin-polarized (top) and valley-polarized (bottom) ground states.

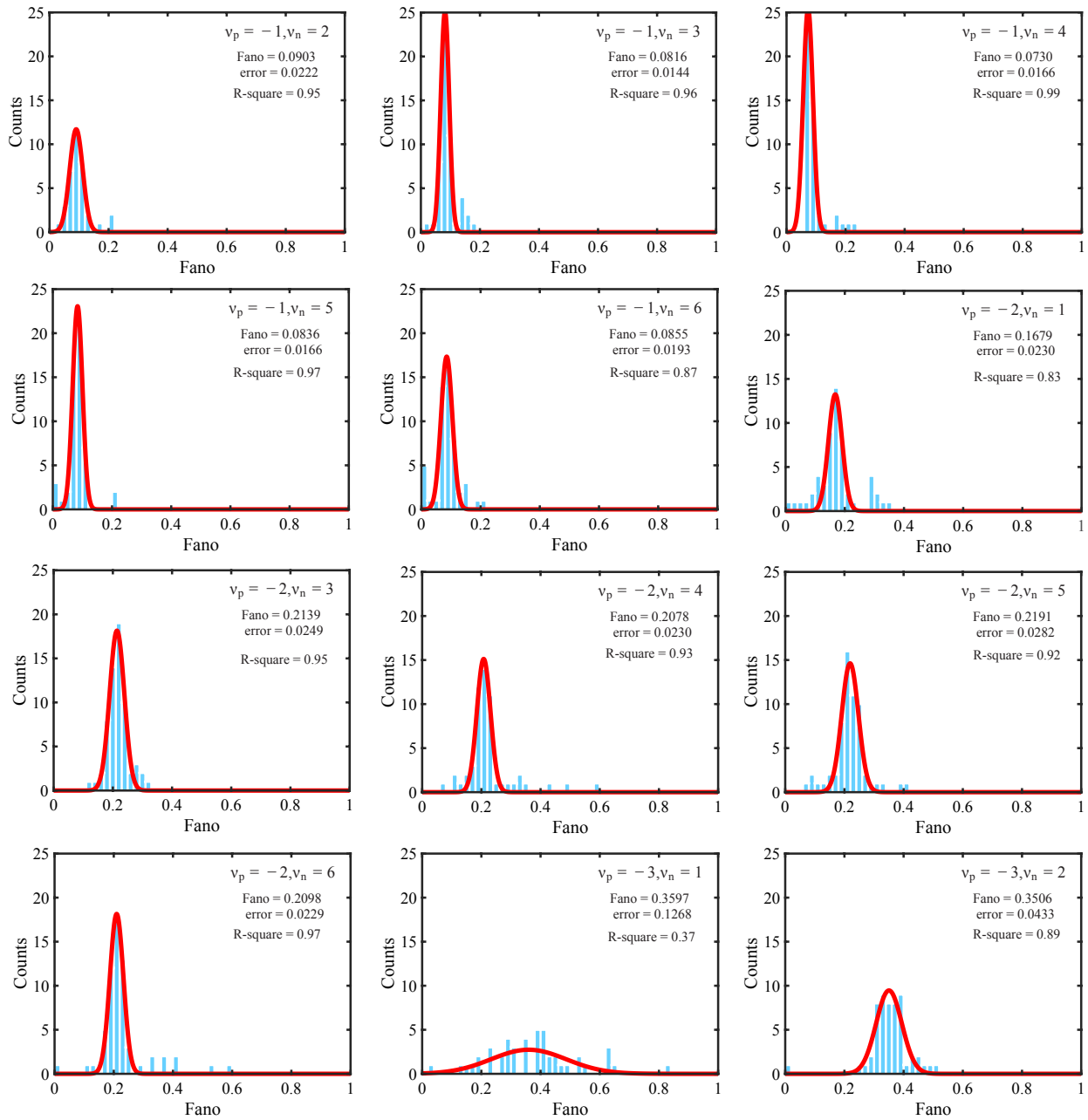**Supplementary Note 5 : Histogram for different plateaus**

As mentioned in the main text, to achieve statistics we have taken multiple noise data (~ 50) on each filling factor plateau, at different gate voltage (V_{BG1}, V_{BG2}) values and from each of these noise data Fano factor have been extracted out. Then we plot the Extracted Fano values for a particular plateau as histogram. In Supplementary Figure 6 and 7, we have shown the histogram of Fano, for different filling factor plateaus. In most of the cases the histogram peaks around a mean value, with a spread depending on the plateaus. The Gaussian fits used to find the mean value of Fano and its standard deviation (error), are shown as red solid line in each plot. The R-square value is to show the preciseness of the Gaussian fit in explaining the variation of Fano.

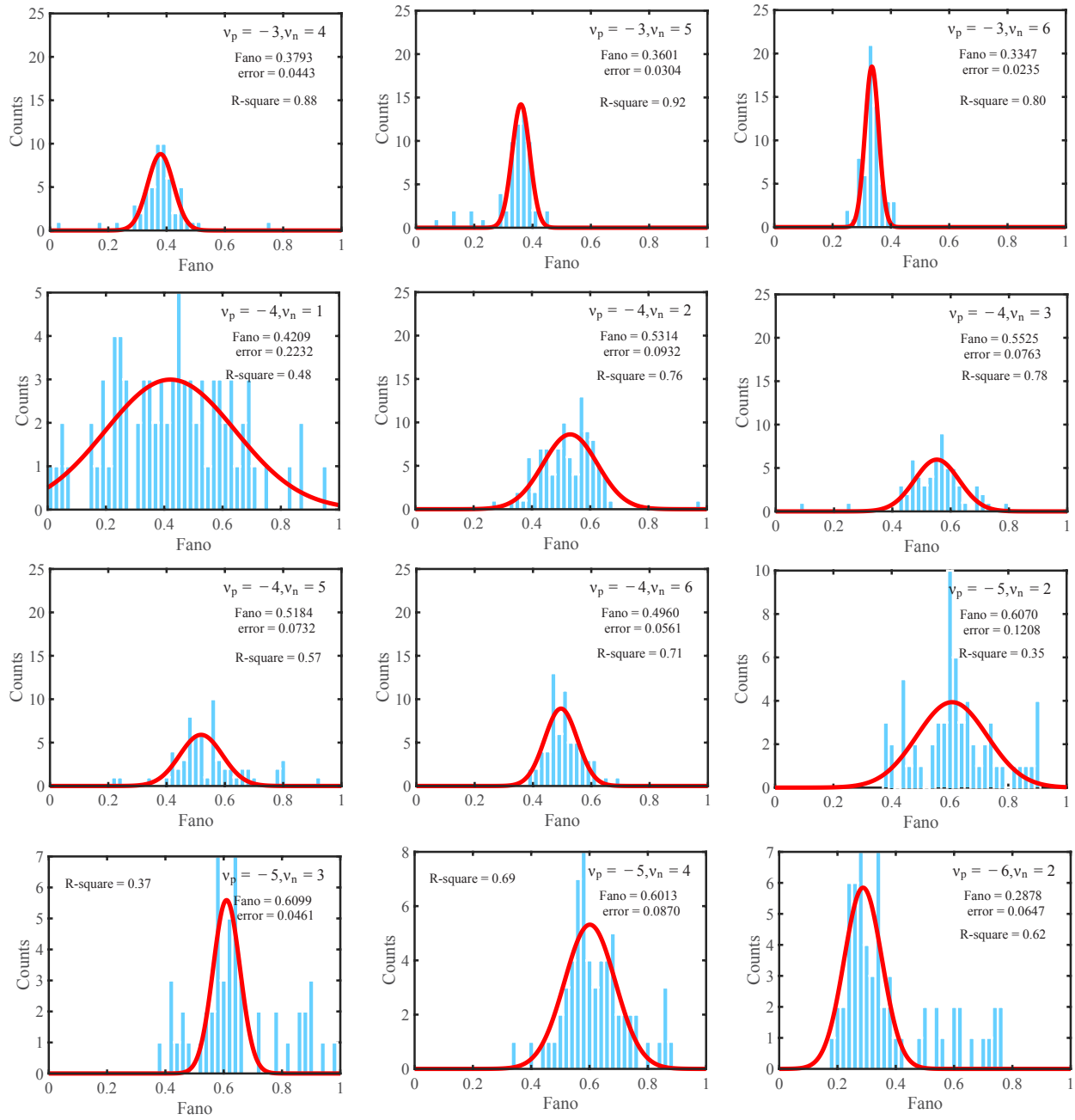**Supplementary Note 6 : Gain calibration of the amplifier chain**

The gain of the HEMT cryo-amplifier changes with temperature cycle. Thus it is essential to check the amplifier gain each time before doing the actual shot noise measurement. In this work, to determine the the total gain of the CA-RTA amplifier chain during measurement, we have utilized the thermal noise of the $\nu_p = -2$ filling factor plateau as shown in Supplementary Figure 8(a). The setup for this is shown in the inset of Supplementary Figure 8(b). As shown, the $BG1$ gated side was maintained in insulating state ($V_{BG1} = -0.1V$), while the $BG2$ gated side was maintained at middle of $\nu_p = -2$ ($V_{BG2} = -0.56V$) filling factor plateau. Since there is no excitation current any voltage fluctuation detected by the measurement circuit is the thermal noise of the quantum resistance for $\nu_p = -2$ filling factor together with background noise and noise from the cold amplifier. For any resistance R, the thermal noise at temperature T is given by $S_V = 4K_BTR = < \delta V_{out} >^2 /(BW * A^2)$, where K_B is the Boltzmann constant and with increasing temperature of the mixing chamber only thermal noise will increase and from the slope one can find the total gain. Supplementary Figure 8(a) shows the frequency response of the thermal noise for different temperatures. Here δV_{out}^2 plotted as function of frequency, shows a peak around $\sim 765kHz$ (resonant frequency of the LC circuit) for all temperatures. Supplementary Figure 8(b) shows $< \delta V_{out}(T) >^2 /BW$ measured at the resonance frequency, , increases linearly with T, as expected. The data is then fitted to determine the slope, from which the effective gain (A) of the amplifier chain is determined as $A = \sqrt{slope/(4K_BR)}$.
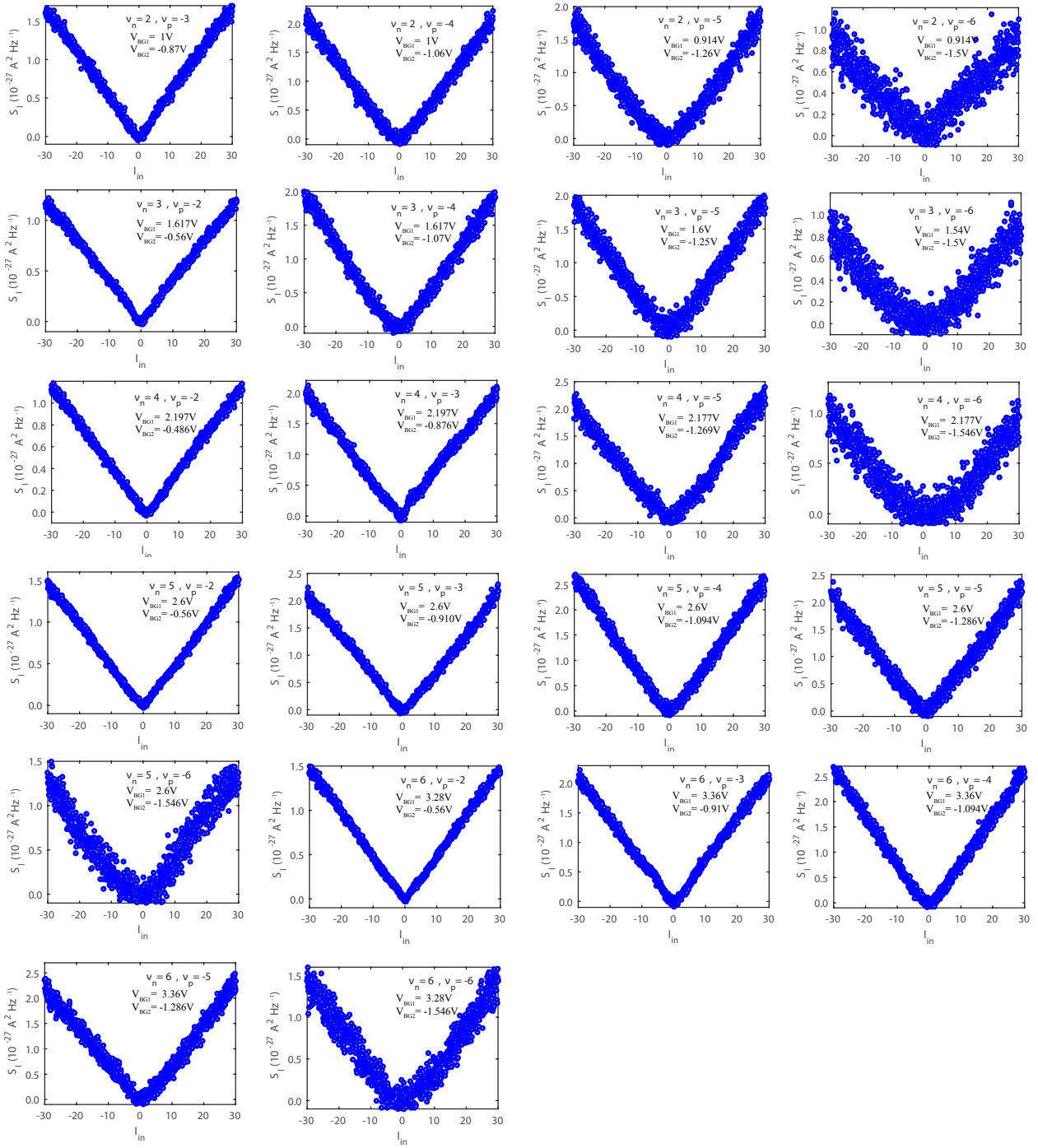
Supplementary Figure 5   Noise data. Single representative noise data for different filling factor (ν_p, ν_n) plateaus, in the bipolar regime. As can be seen from the figures that the S_I increases linearly as a function of I_{in} as expected for shot noise. The gate voltage values at which the data have been taken are shown in the figures.

6

Supplementary Figure 6   Part A: Histogram of Fano for different combination of filling factors in the bipolar regime.

Supplementary Figure 7   part B: Histogram of Fano for different combination of filling factors in the bipolar regime.
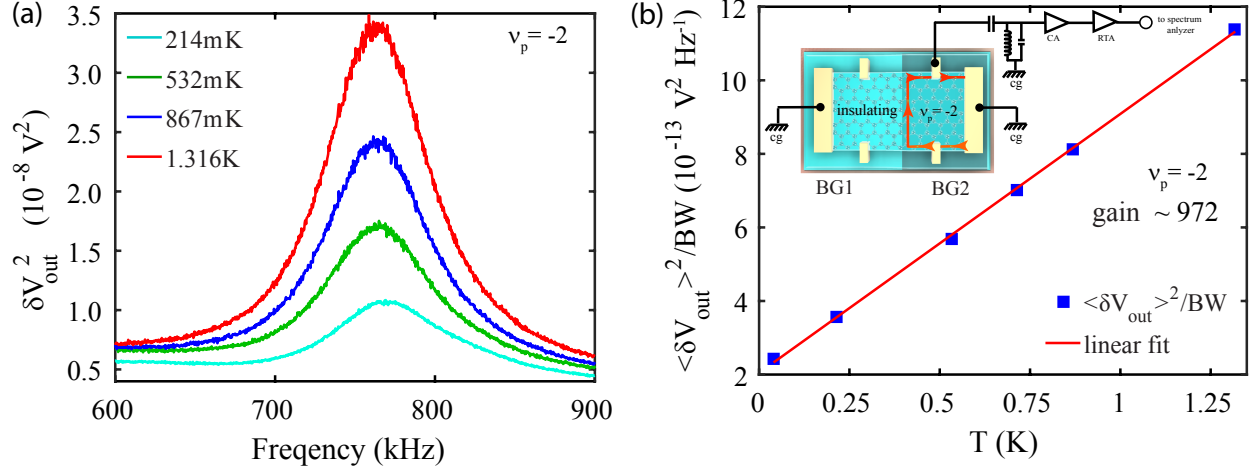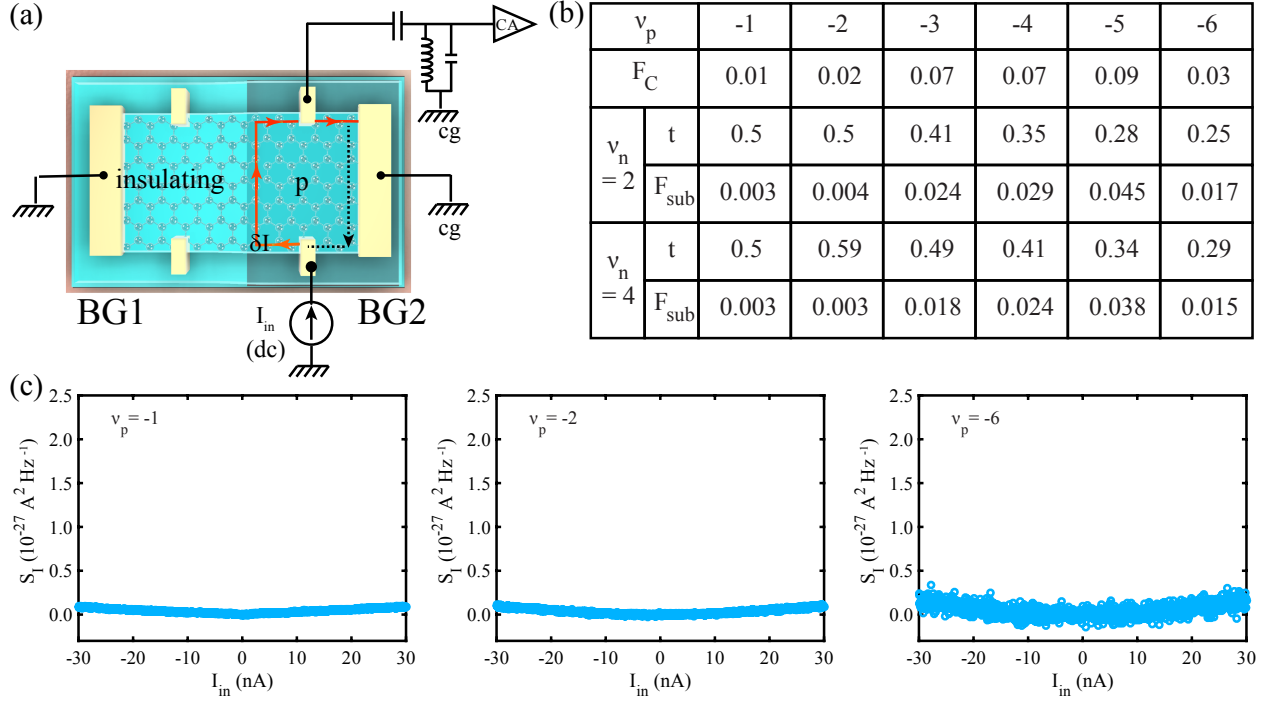
Supplementary Figure 8   **Gain calibration.** (a) Square of voltage fluctuation (δV_{out}^2) due to thermal noise as a function of measurement frequency, at filling factor $\nu_p = -2$ quantum Hall plateau for different temperature. The plots shows a peak around $\sim 765kHz$, which is the resonance frequency of the LC circuit. (b) The measured $< \delta V_{out}(T) >^2 /BW$ or $S_V * A^2$ at the resonance frequency as function of temperature. Red line is the linear fit to find the slope in order to determine the total gain (~ 972). The inset shows the thermal noise measurement configuration.

The effective gain of the amplifier chain was found to be around ~ 972, which was utilized for all the noise analysis, shown in this work.

## Supplementary Note 7 : Contact noise measurement

The Supplementary Figure 9(a) shows the set up to measure contact noise, where the left side of the pn junction is kept at insulating state, so that there is no noise due to the pn junction. There are two possible sources of contact noise: 1) Unwanted noise (shown by δI in Supplementary Figure 9(a)) generated from the current injection probe due to finite contact resistance and 2) unwanted noise (shown by the black dashed line in Supplementary Figure 9(a)) due to the reflection of current from the right cold ground again due to finite contact resistance. Supplementary Figure 9(c) shows some of the contact noise data for different p side filling factors. As can be seen from the figures that maximum value of contact noise is one order smaller in magnitude compared to the noise generated at the pn junction. In Supplementary Figure 9(b) table, the Fano values extracted from the contact noise data (F_C) are shown. However, in the noise measurement of the pn junction, some part of the generated contact noise transmits to n side and the transmitted contact noise to p side is $(1-t)^2 F_C$. In our final analysis we have subtracted $F_{sub} = (1-t)^2 F_C$ from the noise data presented in the manuscript. In the Supplementary Figure 9(b) table we have also quoted the values of F_{sub} for $\nu_n = 2$ and $\nu_n = 4$.

(a) (b) (c)

ν_p		-1	-2	-3	-4	-5	-6
	F_C	0.01	0.02	0.07	0.07	0.09	0.03
$\nu_n = 2$	t	0.5	0.5	0.41	0.35	0.28	0.25
	F_{sub}	0.003	0.004	0.024	0.029	0.045	0.017
$\nu_n = 4$	t	0.5	0.59	0.49	0.41	0.34	0.29
	F_{sub}	0.003	0.003	0.018	0.024	0.038	0.015

Supplementary Figure 9   Contact noise. (a) Experimental setup to measure contact noise. Noise introduced by the current injection probe (δI) and partitioning noise due to imperfect nature of the right ground are the two possible source of contact noise. During contact noise measurement the $BG1$ side is maintained in insulating state. (b) Fano factor (F_C) determined from the contact noise data taken at different p side filling factors, while the other side of the pn junction is maintained at insulating state. When the other side of the junction is not in insulating state, the contact noise contribution is further reduced to $F_{sub} = (1 - t)^2 F_C$, which has been shown for filling factor $\nu_n = 2$ and $\nu_n = 4$ (c) Representative contact noise data for different values of ν_p. The maximum value of the contact noise is one order smaller than the noise generated by the pn junction.

Supplementary Note 8 : Filling factor dependence of Fano

The dependence of experimentally measured F with increasing ν_n and ν_p are shown in figure Supplementary Figure 10 and Supplementary Figure 11, respectively. We have compared the experimental data with spin-selective equilibration model for both spin-polarized and valley-polarized spin sequence of the co-propagating edge states as described in Supplementary Figure 4. For the spin-polarized case, the solid red and black lines show the theoretical Fano values for coherent and incoherent (quasi-elastic) scattering, respectively. The blue and sky color dashed lines show the same for the valley-polarized case. The two different spin sequence gives very similar values as can be seen from the figures. The errorbars are color-coded according to the R-square value of the Gaussian fits of the histograms.
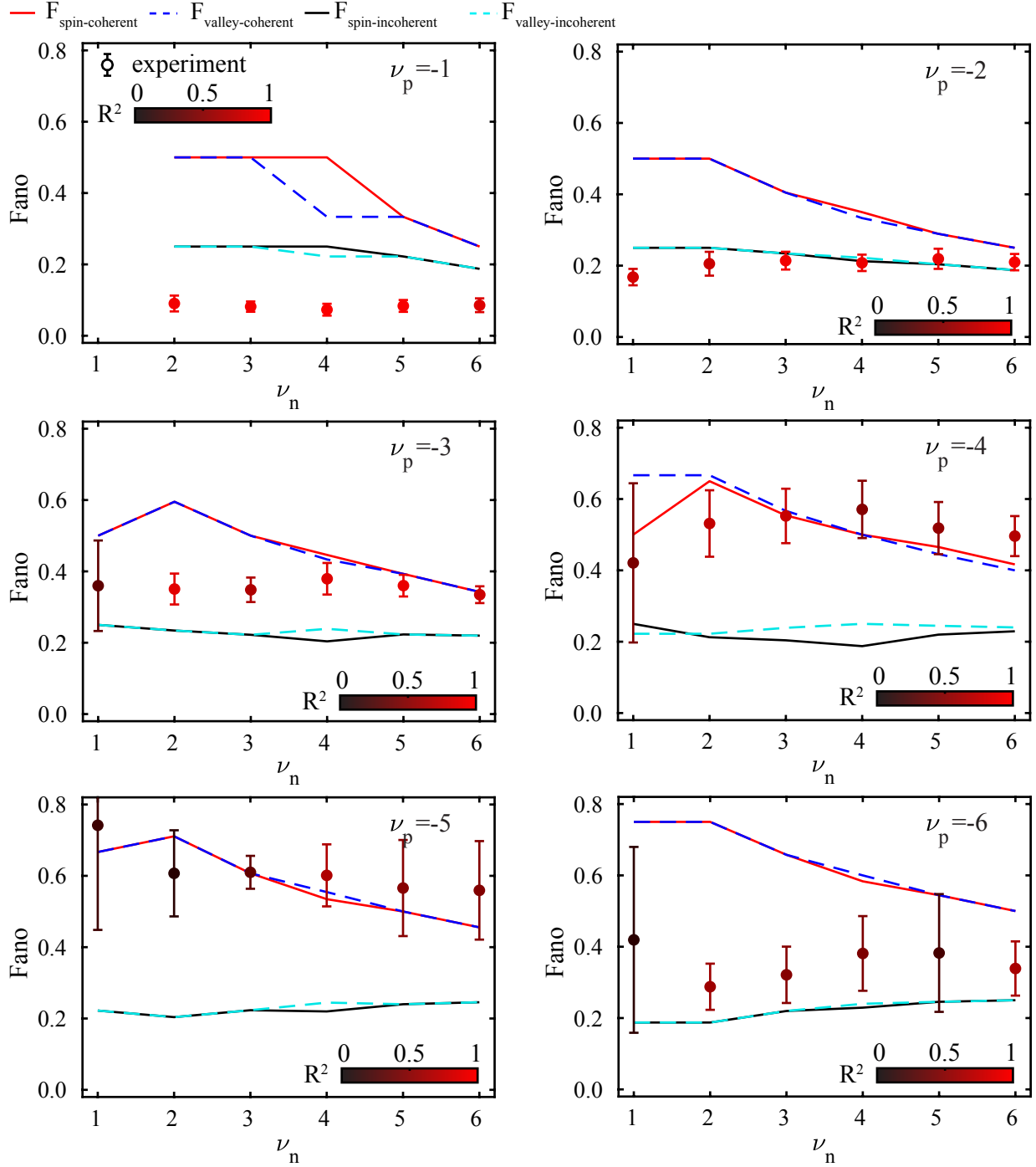
Supplementary Figure 10   Fano versus ν_n. The experimental Fano (F_{exp}) as function of n-side filling factor ν_n for fixed p-side filling factor ν_p, is shown by open circles with errorbars. For spin-selective equilibration with spin structure of spin-polarized ground state, the Fano for coherent ($F_{spin-coherent}$) and incoherent ($F_{spin-incoherent}$)cases are shown in red and black solid lines. Similarly blue and sky colored dashed lines shows Fano values ($F_{valley-coherent}$ and $F_{valley-incoherent}$, respectively) for the case of valley-polarized ground state. The color of the error bar shows the preciseness of the corresponding Gaussian fitting of Fano histogram, in terms of R-square.
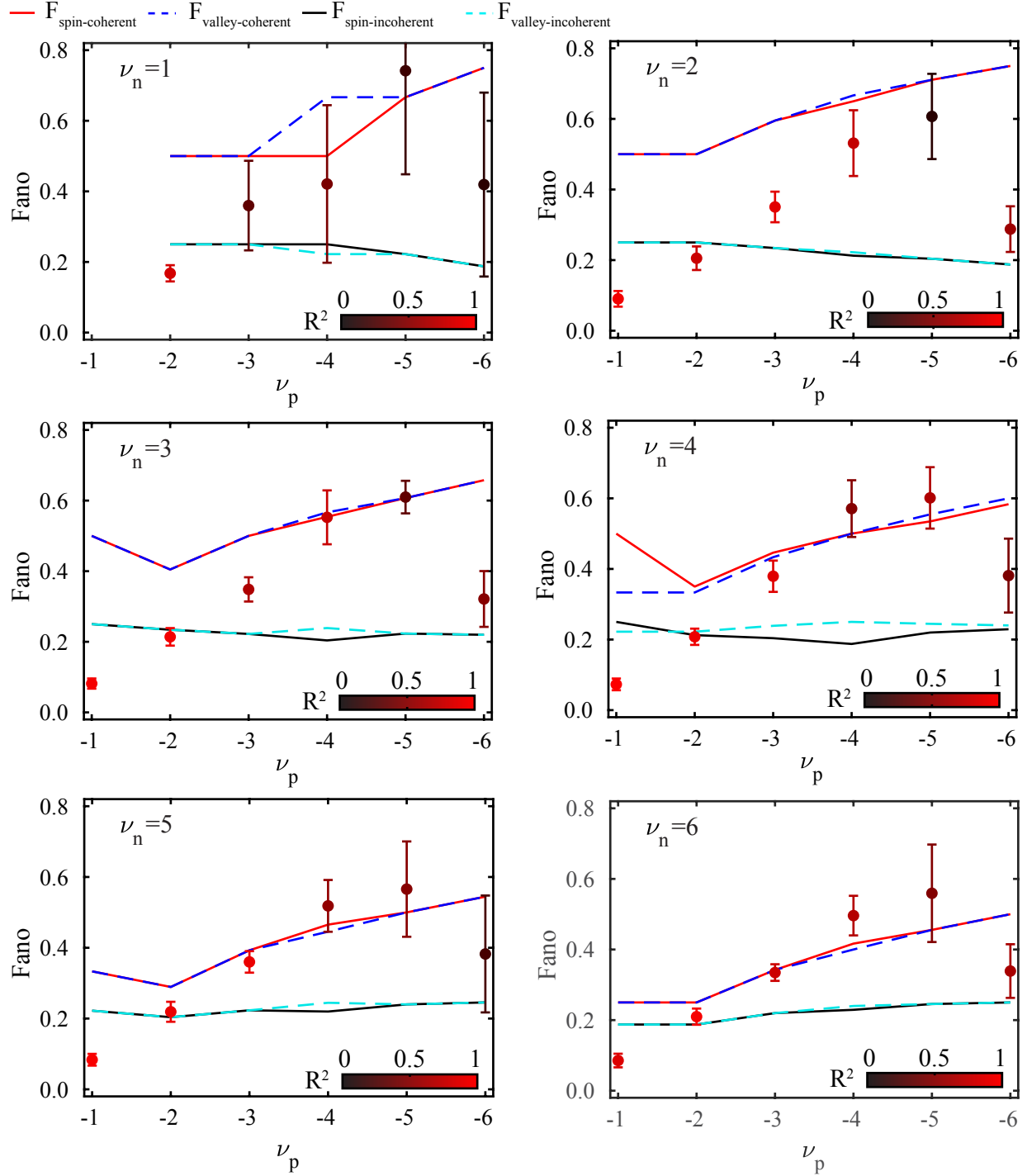
Supplementary Figure 11 **Fano versus** ν_p. The experimental Fano (F_{exp}) as function of p-side filling factor ν_p for fixed n-side filling factor ν_n, is shown by open circles with errorbars. For spin-selective equilibration with spin structure of spin-polarized ground state, the Fano for coherent ($F_{spin-coherent}$) and incoherent ($F_{spin-incoherent}$) cases are shown in red and black solid lines. Similarly blue and sky colored dashed lines shows Fano values ($F_{valley-coherent}$ and $F_{valley-incoherent}$, respectively) for the case of valley-polarized ground state. The color of the error bar shows the preciseness of the corresponding Gaussian fitting of Fano histogram, in terms of R-square.

Supplementary Note 9 : Derivation of F using theoretical model

Scattering Matrix approach for coherent scattering : Following scattering matrix approach given in ref. [5] and [6], we derive general expression of F for coherent scattering considering pn junction as fictitious contact as described in details ref. [5] and [4]. This fictitious contact model is shown in Supplementary Figure 12. In Supplementary Figure 12(a) the current distribution of actual device is shown, where current injected at contact 1 is partitioned at the junction and the transmitted and reflected current respectively goes to contact 2 and 3. The equivalent scattering model is shown for filling factors $(\nu_p, \nu_n) = (-2, 3)$, in Supplementary Figure 12(b). Here it is assumed that the scattering probability (ϵ) from any edge state to all the other co-propagating edge state is same. Since the experimental data was taken on the reflection side we need to evaluate the current noise spectral density at contact 3. As given in ref. [6], at zero temperature limit for a multi-terminal device the correlation term of current fluctuation $S_{\alpha\beta}(=< \delta I_\alpha \delta I_\beta >)$ between two contacts α and β is given by:

$$S_{\alpha\beta} = 2\frac{e^2}{h} \sum_{\gamma\lambda,\gamma\neq\lambda} \int dE Tr(s_{\alpha\gamma}^\dagger s_{\alpha\lambda} s_{\beta\lambda}^\dagger s_{\beta\gamma}) f_\gamma(1 - f_\lambda) \tag{1}$$

where s_{mn} are scattering matrices, with elements $s_{mk,ni}$, which indicates the probability of an electron injected at ith edge state from contact n, to scatter into the kth edge state going into contact m and f_λ and f_γ are the zero temperature Fermi distribution function of contact λ and γ, respectively. The noise spectral density at contact α is given by the autocorelation term:

$$S_{\alpha\alpha} = 2\frac{e^2}{h} \sum_{\gamma\lambda,\gamma\neq\lambda} \int dE Tr(s_{\alpha\gamma}^\dagger s_{\alpha\lambda} s_{\alpha\lambda}^\dagger s_{\alpha\gamma}) f_\gamma(1 - f_\lambda). \tag{2}$$

Thus for our case the noise carried by the reflected edges from pn junction is given by S_{33} (see Supplementary Figure 12), for which the trace of the matrices $s_{3\gamma}^\dagger s_{3\lambda} s_{3\lambda}^\dagger s_{3\gamma}$ needs to be determined first. However, at zero temperature limit most of the γ,λ combination term inside the integration of Eqn. 2 goes to zero due to the term $f_\gamma(1 - f_\lambda)$ and following the scattering matrix approach in ref. [5, 6, 7] the only surviving term is $s_{31}^\dagger s_{32} s_{32}^\dagger s_{31}$. The corresponding integration term with $f_1(1 - f_2)$ is equal to eV_{sd}. As example we have shown the $s_{31}^\dagger s_{32} s_{32}^\dagger s_{31}$ matrix and derived S_{33} from Eqn. 2 for (-1,1), (-2,2) and (-1,3) filling factors in Supplementary Figure 13, 14 and 15, respectively. Similarly derived expression of different filling factors is summarized in Supplementary Table 1, where it can be seen that S_{33} follows a general expression $S_{33} = 2eI_{in}T(1-T)$, where T is the average transmittance. Therefore for coherent scattering process Fano factor is given by: $F = (1 - T)$.

filling factors	S_{33}	I_t	Fano
(-1,1)	$2\frac{e^2}{h}eV_{sd}\epsilon(1-\epsilon) = 2eI_{in}\epsilon(1-\epsilon)$	ϵI_{in}	$(1-\epsilon)$
(-1,2)	$2\frac{e^2}{h}eV_{sd}2\epsilon(1-2\epsilon) = 2eI_{in}2\epsilon(1-2\epsilon)$	$2\epsilon I_{in}$	$(1-2\epsilon)$
(-1,3)	$2\frac{e^2}{h}eV_{sd}3\epsilon(1-3\epsilon) = 2eI_{in}3\epsilon(1-3\epsilon)$	$3\epsilon I_{in}$	$(1-3\epsilon)$
(-2,1)	$2\frac{e^2}{h}eV_{sd}2\epsilon(1-\epsilon) = 2eI_{in}\epsilon(1-\epsilon)$	ϵI_{in}	$(1-\epsilon)$
(-2,2)	$2\frac{e^2}{h}eV_{sd}4\epsilon(1-2\epsilon) = 2eI_{in}2\epsilon(1-2\epsilon)$	$2\epsilon I_{in}$	$(1-2\epsilon)$
(-2,3)	$2\frac{e^2}{h}eV_{sd}6\epsilon(1-3\epsilon) = 2eI_{in}3\epsilon(1-3\epsilon)$	$3\epsilon I_{in}$	$(1-3\epsilon)$

**Supplementary Table 1 : Fano for coherent scattering**
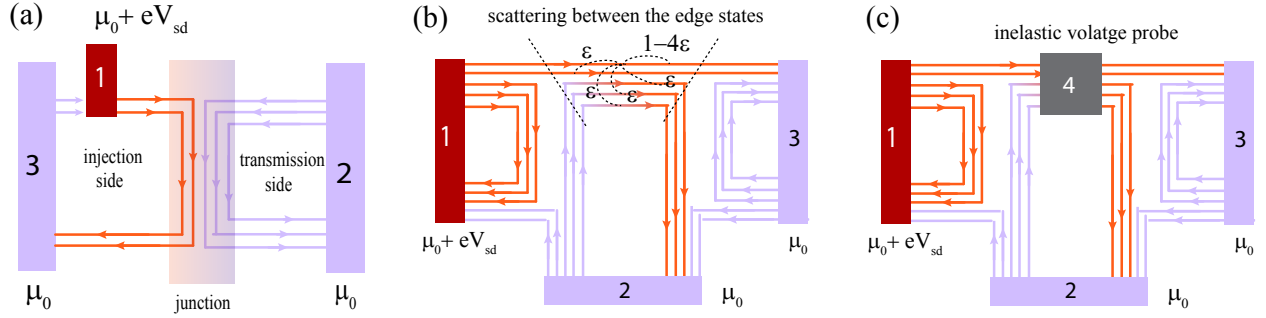
Supplementary Figure 12 Fictitious contact model. (a) The current distribution of the real device. Current is injected at contact 1 and after partitioning, reflected and transmitted current goes to contact 3 and 2 respectively. (b) Equivalent model with pn junction as the fictitious contact for coherent scattering. At the fictitious contact the scattering probability (ϵ) of a charge carrier from one edge state to any any other is equal. (c) Equivalent model for incoherent scattering.
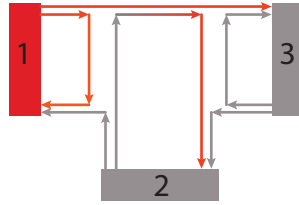
$$s_{31}^\dagger s_{32} s_{32}^\dagger s_{31} = \begin{bmatrix} i\sqrt{1-\epsilon} & 0 \\ 0 & 0 \end{bmatrix} \begin{bmatrix} 0 & \sqrt{\epsilon} \\ 0 & 0 \end{bmatrix} \begin{bmatrix} 0 & 0 \\ \sqrt{\epsilon} & 0 \end{bmatrix} \begin{bmatrix} -i\sqrt{1-\epsilon} & 0 \\ 0 & 0 \end{bmatrix} = \begin{bmatrix} \epsilon(1-\epsilon) & 0 \\ 0 & 0 \end{bmatrix}$$

$$S_{33} = 2\frac{e^2}{h}eV_{sd}\epsilon(1-\epsilon) = 2eI_{in}\epsilon(1-\epsilon)$$

Supplementary Figure 13 Scattering matrices and auto-correlation term S_{33} for $\nu_p = -1$ and $\nu_n = 1$:
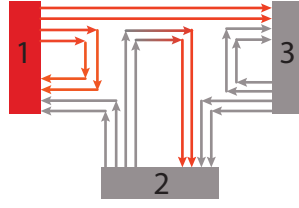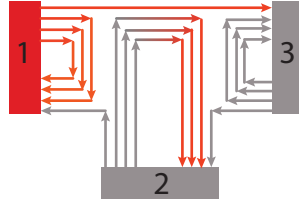
$$s_{31}^{\dagger} s_{32} s_{32}^{\dagger} s_{31} = \begin{bmatrix} i\sqrt{1-\epsilon} & \sqrt{\epsilon} & 0 & 0 \\ \sqrt{\epsilon} & i\sqrt{1-\epsilon} & 0 & 0 \\ 0 & 0 & 0 & 0 \\ 0 & 0 & 0 & 0 \end{bmatrix} \begin{bmatrix} 0 & 0 & \sqrt{\epsilon} & \sqrt{\epsilon} \\ 0 & 0 & \sqrt{\epsilon} & \sqrt{\epsilon} \\ 0 & 0 & 0 & 0 \\ 0 & 0 & 0 & 0 \end{bmatrix} \begin{bmatrix} 0 & 0 & 0 & 0 \\ 0 & 0 & 0 & 0 \\ \sqrt{\epsilon} & \sqrt{\epsilon} & 0 & 0 \\ \sqrt{\epsilon} & \sqrt{\epsilon} & 0 & 0 \end{bmatrix}$$

$$X \begin{bmatrix} -i\sqrt{1-\epsilon} & \sqrt{\epsilon} & 0 & 0 \\ \sqrt{\epsilon} & -i\sqrt{1-\epsilon} & 0 & 0 \\ 0 & 0 & 0 & 0 \\ 0 & 0 & 0 & 0 \end{bmatrix} = \epsilon \begin{bmatrix} 2(1-2\epsilon) & 2(1-2\epsilon) & 0 & 0 \\ 2(1-2\epsilon) & 2(1-2\epsilon) & 0 & 0 \\ 0 & 0 & 0 & 0 \\ 0 & 0 & 0 & 0 \end{bmatrix}$$

$$S_{33} = 2\frac{e^2}{h} eV_{sd} 4\epsilon(1-2\epsilon) = 2eI_{in} 2\epsilon(1-2\epsilon)$$

Supplementary Figure 14 Scattering matrices and auto-correlation term S_{33} for $\nu_p = -2$ and $\nu_n = 2$:
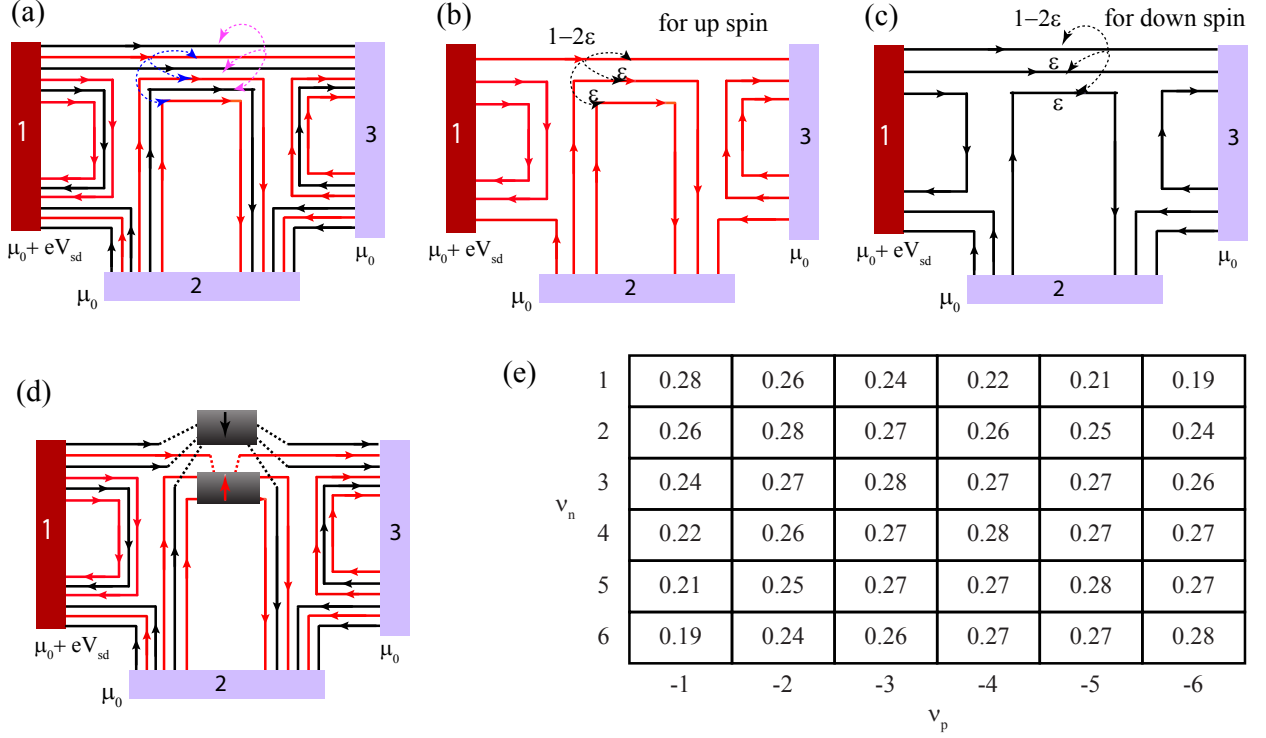

$$s_{31}^{\dagger} s_{32} s_{32}^{\dagger} s_{31} = \begin{bmatrix} i\sqrt{1-\epsilon} & 0 & 0 & 0 \\ 0 & 0 & 0 & 0 \\ 0 & 0 & 0 & 0 \\ 0 & 0 & 0 & 0 \end{bmatrix} \begin{bmatrix} 0 & \sqrt{\epsilon} & \sqrt{\epsilon} & \sqrt{\epsilon} \\ 0 & 0 & 0 & 0 \\ 0 & 0 & 0 & 0 \\ 0 & 0 & 0 & 0 \end{bmatrix} \begin{bmatrix} 0 & 0 & 0 & 0 \\ \sqrt{\epsilon} & 0 & 0 & 0 \\ \sqrt{\epsilon} & 0 & 0 & 0 \\ \sqrt{\epsilon} & 0 & 0 & 0 \end{bmatrix}$$

$$X \begin{bmatrix} -i\sqrt{1-\epsilon} & 0 & 0 & 0 \\ 0 & 0 & 0 & 0 \\ 0 & 0 & 0 & 0 \\ 0 & 0 & 0 & 0 \end{bmatrix} = 3\epsilon(1-3\epsilon) \begin{bmatrix} 1 & 0 & 0 & 0 \\ 0 & 0 & 0 & 0 \\ 0 & 0 & 0 & 0 \\ 0 & 0 & 0 & 0 \end{bmatrix}$$

$$S_{33} = 2\frac{e^2}{h} eV_{sd} 3\epsilon(1-3\epsilon) = 2eI_{in} 3\epsilon(1-3\epsilon)$$

Supplementary Figure 15   Scattering matrices and auto-correlation term S_{33} for $\nu_p = -1$ and $\nu_n = 3$:

Supplementary Figure (e) table:

ν_n	-1	-2	-3	-4	-5	-6
1	0.28	0.26	0.24	0.22	0.21	0.19
2	0.26	0.28	0.27	0.26	0.25	0.24
3	0.24	0.27	0.28	0.27	0.27	0.26
4	0.22	0.26	0.27	0.28	0.27	0.27
5	0.21	0.25	0.27	0.27	0.28	0.27
6	0.19	0.24	0.26	0.27	0.27	0.28

ν_p

Supplementary Figure 16 (a) Fictitious contact model for spin selective equilibration for filling factor $(-3, 3)$. The up and down spin edge channels are shown by red and black arrow lines, respectively. (b) Model only for the up spin edge channel and (c) is the same for down spin edge channel (d) Parallel voltage probe model for quasi-elastic scattering (e) Fano for inelastic scattering as function of filling factor.

Now we consider the case of spin selective equilibration of the edge states. In Supplementary Figure 16(a), we have shown the fictitious contact model for filling factor $(-3, 3)$ with broken spin degeneracy. As there is no scattering between opposite spin edge states the matrix elements $s_{mk,ni}$ corresponding to inter-spin scattering probability are zero. This essentially separates out the noise contribution for each spin channel as depicted in Supplementary Figure 16(b) and 16(c), where the model for filling factor $(-3, 3)$ can be considered as a super-position of filling factor $(-2, 1)$ for up spin (Supplementary Figure 16(b)) and $(-1, 2)$ for down spin (Supplementary Figure 16(c)). As a result the auto correlation term for the spin selective case can be written as:

$$S_{\alpha\alpha} = 2\frac{e^2}{h} \sum_{\gamma\lambda,\gamma\neq\lambda} \int dE Tr(s_{\alpha\gamma}^\dagger s_{\alpha\lambda} s_{\alpha\lambda}^\dagger s_{\alpha\gamma})^\uparrow f_\gamma(1-f_\lambda) + 2\frac{e^2}{h} \sum_{\gamma\lambda,\gamma\neq\lambda} \int dE Tr(s_{\alpha\gamma}^\dagger s_{\alpha\lambda} s_{\alpha\lambda}^\dagger s_{\alpha\gamma})^\downarrow f_\gamma(1-f_\lambda).$$

(3)

where the up and down arrow index corresponds to matrix element of only up spin and down spin channels, respectively. It can be seen immediately from eqn. 3 that for the filling factor $(-3, 3)$ the auto correlation term takes the form:

$$S_{33} = 2\frac{e^2}{h}eV_{sd}2\epsilon(1-\epsilon) + 2\frac{e^2}{h}eV_{sd}2\epsilon(1-2\epsilon) = 2eI_{in\uparrow}\epsilon(1-\epsilon) + 2eI_{in\downarrow}2\epsilon(1-2\epsilon) \qquad (4)$$

16

The equation 4 can be further generalized for other filling factor combinations as:

$$S_{33} = S_I = 2eI_{in\uparrow}t_\uparrow F_\uparrow + 2eI_{in\downarrow}t_\downarrow F_\downarrow = 2eI_{t\uparrow}F_\uparrow + 2eI_{t\downarrow}F_\downarrow \tag{5}$$

where $t_\uparrow$ and $t_\downarrow$ are the transmittance and $F_\uparrow$ and $F_\downarrow$ are the Fano factors associated with up spin and down spin channel. Now following the discussion for spin selective equilibration in Supplementary Note 4, putting $I_{in\uparrow} = (|\nu_{p\uparrow}/\nu_p|)I_{in}$ and $I_{in\downarrow} = (|\nu_{p\downarrow}/\nu_p|)I_{in}$ in eqn. 5, the expression for shot noise becomes:

$$S_I = 2eI_{in}(1/|\nu_p|)[t_\uparrow|\nu_{p\uparrow}|F_\uparrow + t_\downarrow|\nu_{p\downarrow}|F_\downarrow] \tag{6}$$

The Fano factor is conventionally defined as $F = S_I/2eI_t = S_I/2etI_{in}$. Thus considering the expression of t for spin selective equlibration the effective Fano takes the general form:

$$F = \frac{t_\uparrow|\nu_{p\uparrow}|F_\uparrow + t_\downarrow|\nu_{p\downarrow}|F_\downarrow}{t_\uparrow|\nu_{p\uparrow}| + t_\downarrow|\nu_{p\downarrow}|} \tag{7}$$

As we have derived earlier for coherent scattering $F_\uparrow = 1 - t_\uparrow$ and $F_\downarrow = 1 - t_\downarrow$, hence:

$$F = \frac{|\nu_{p\uparrow}|t_\uparrow(1 - t_\uparrow) + |\nu_{p\downarrow}|t_\downarrow(1 - t_\downarrow)}{t_\uparrow|\nu_{p\uparrow}| + t_\downarrow|\nu_{p\downarrow}|} \tag{8}$$

We have used eqn. 8 to calculate the Fano factor for coherent scattering considering full equilibration among the same type of spin channels at the pn junction i.e for $t_\uparrow = |\nu_{n\uparrow}|/(|\nu_{n\uparrow}| + |\nu_{p\uparrow}|)$ and $t_\downarrow = |\nu_{n\downarrow}|/(|\nu_{n\downarrow}| + |\nu_{p\downarrow}|)$.

Fano for incoherent scattering: For the incoherent scattering, first we will discuss the quasi-elastic process as described in ref. [4, 8, 9] based on random matrix theory, and $F = |\nu_p\nu_n|/(|\nu_p| + |\nu_n|)^2 = t(1 - t)$, where $t = |\nu_n|/(|\nu_p| + |\nu_n|)$ considering full equilibration. In the fictitious contact model, the effect of incoherent scattering (quasielastic or inelastic process) are introduced by adding a 4th volatge probe [4, 5] along which the scattering happens as shown in Supplementary Figure 12(c). In case of spin selective equilibration two parallel voltage probes can be introduced for the up spin and down spin channels as shown in Supplementary Figure 16(d), for quasielastic scattering. Since the voltage fluctuation of these two probes are independent of each other, the Fano expression of eqn. 7 for coherent scattering can be extended to the quasielastic case considering similar matrix element arguments used for the coherent case. Thus for spin selective equilibration with quasi elastic scattering the Fano for up and down spin channels are given by $F_\uparrow = t_\uparrow(1 - t_\uparrow)$ and $F_\downarrow = t_\downarrow(1 - t_\downarrow)$, respectively. Therefore, the Fano can be expressed as

$$F = \frac{|\nu_{p\uparrow}|t_\uparrow^2(1 - t_\uparrow) + |\nu_{p\downarrow}|t_\downarrow^2(1 - t_\downarrow)}{t_\uparrow|\nu_{p\uparrow}| + t_\downarrow|\nu_{p\downarrow}|} \tag{9}$$

We have compared our experimental data with the Fano values calculated using eqn. 9 for quasielastic based incoherent scattering.

For inelastic based incoherent scattering, the charge carriers can exchange energy. As a result, the energy distribution of the carriers can be characterized by an effective temperature T_{eff} [8], which is determined by the balance of the energy supplied from the reservoirs and electron thermal energy flowing out, and the the Fano is given by $F' = (1/\pi)\sqrt{3F}$, where F is the Fano for the quasielastic case. This also means that the parallel voltage probe model considered for the quasi-elastic case becomes invalid if

inelastic process are present. For this reason in Supplementary Figure 16(e) we have shown the calculated Fano values for inelastic process as a function of filling factor, considering full equilibration of all the edge channels. Note that these values are very similar to the quasielastic case. For simplicity we have only compared the experimental data with the spin selective coherent scattering and quasielastic scattering in the main manuscript and in the Supplementary information.

Supplementary References :

1. Pizzocchero, F. *et al.* The hot pick-up technique for batch assembly of van der waals heterostructures. *Nature communications* **7**, 1–10 (2016).

2. Purdie, D. *et al.* Cleaning interfaces in layered materials heterostructures. *Nature communications* **9**, 5387 (2018).

3. Zomer, P., Guimarães, M., Brant, J., Tombros, N. & Van Wees, B. Fast pick up technique for high quality heterostructures of bilayer graphene and hexagonal boron nitride. *Applied Physics Letters* **105**, 013101 (2014).

4. Kumada, N., Parmentier, F., Hibino, H., Glattli, D. & Roulleau, P. Shot noise generated by graphene p–n junctions in the quantum hall effect regime. *Nature communications* **6**, 8068 (2015).

5. Texier, C. & Büttiker, M. Effect of incoherent scattering on shot noise correlations in the quantum hall regime. *Physical Review B* **62**, 7454 (2000).

6. Büttiker, M. Scattering theory of current and intensity noise correlations in conductors and wave guides. *Physical Review B* **46**, 12485 (1992).

7. Blanter, Y. M. & Büttiker, M. Shot noise in mesoscopic conductors. *Physics reports* **336**, 1–166 (2000).

8. Abanin, D. & Levitov, L. Quantized transport in graphene pn junctions in a magnetic field. *Science* **317**, 641–643 (2007).

9. Matsuo, S. *et al.* Edge mixing dynamics in graphene p–n junctions in the quantum hall regime. *Nature communications* **6**, 8066 (2015).